Mixing with applications to inertial-confinement-fusion implosions

V. Rana, H. Lim, J. Melvin, and J. Glimm
Department of Applied Mathematics and Statistics, Stony Brook University, Stony Brook, New York 11794-3600, USA

B. Cheng and D. H. Sharp
Los Alamos National Laboratory, Los Alamos, New Mexico 87545, USA

(Received 15 January 2016; revised manuscript received 23 August 2016; published 9 January 2017)

Approximate one-dimensional (1D) as well as 2D and 3D simulations are playing an important supporting role in the design and analysis of future experiments at National Ignition Facility. This paper is mainly concerned with 1D simulations, used extensively in design and optimization. We couple a 1D buoyancy-drag mix model for the mixing zone edges with a 1D inertial confinement fusion simulation code. This analysis predicts that National Ignition Campaign (NIC) designs are located close to a performance cliff, so modeling errors, design features (fill tube and tent) and additional, unmodeled instabilities could lead to significant levels of mix. The performance cliff we identify is associated with multimode plastic ablator (CH) mix into the hot-spot deuterium and tritium (DT). The buoyancy-drag mix model is mode number independent and selects implicitly a range of maximum growth modes. Our main conclusion is that single effect instabilities are predicted not to lead to hot-spot mix, while combined mode mixing effects are predicted to affect hot-spot thermodynamics and possibly hot-spot mix. Combined with the stagnation Rayleigh-Taylor instability, we find the potential for mix effects in combination with the ice-to-gas DT boundary, numerical effects of Eulerian species CH concentration diffusion, and ablation-driven instabilities. With the help of a convenient package of plasma transport parameters developed here, we give an approximate determination of these quantities in the regime relevant to the NIC experiments, while ruling out a variety of mix possibilities. Plasma transport parameters affect the 1D buoyancy-drag mix model primarily through its phenomenological drag coefficient as well as the 1D hydro model to which the buoyancy-drag equation is coupled.

DOI: 10.1103/PhysRevE.95.013203

I. INTRODUCTION

The purpose of this paper is to examine Rayleigh-Taylor (RT) and Richtmyer-Meshkov (RM) mixing in National Ignition Campaign (NIC) fusion capsules, as shown in Fig. 1 in terms of their overall instability growth rates. We couple a one-dimensional (1D) buoyancy-drag mix model for the mixing zone edges to a 1D inertial confinement fusion (ICF) simulation code. The main prediction indicates that the NIC designs are located near a performance cliff—a conclusion which appears to be consistent with experimental data. With regards to post-shot simulations fully consistent with experimental data and laws of physics, it seems that neither the high-foot nor the low-foot simulations have attained this goal. The reference to a performance cliff is a judgment reflected in the observation that the high-foot simulations could be closer to this goal than are the low-foot simulations. A review of the presumably multiple verification and validation issues still relevant for simulation of low- (or high-) foot National Ignition Facility (NIF) experiments is out of the scope of this article. Reference [1] identifies a dominant high-foot performance issue as radiation asymmetry and mentions as a low-foot issue ablation front asymmetries (due to RT instabilities, the tent, and fill tube). The main difference between the NIC low-foot and the high-foot shots is that these instabilities are suppressed in the high-foot shot because of the number of shocks and the smaller Atwood number at the interface. In summary, it is thought that the NIC performance cliff is mainly due to the asymmetry induced by these instabilities.

We analyze several single-cause instability mechanisms and find that the design is stable relative to these effects, but we find that combined mechanisms are more dangerous and have a potential to degrade the performance of NIF fusion capsules.

Input to this analysis is a systematic study of plasma transport parameters, covering the NIC implosion range. In more detail, we find

(1) No multimode CH mix into the NIC hot spot from the RM and stagnation RT instabilities. No significant role is found for concentration diffusion.

(2) Severe mesh requirements for Eulerian simulations to avoid spurious CH mix into the cold shell.

(3) Possible mix of CH into the hot spot from a combination of the RT stagnation instability and laser drive inhomogeneities. Other combined mechanisms may also degrade the NIC performance, especially the temperature of the hot spot at bang time.

Simulations in 1D, 2D, as well as 3D are playing an important role in the design and analysis of future experiments at NIF. We concentrate in this paper on 1D simulations, widely used for design and optimization, augmented with an easy-to-use 1D mix model for the mixing zone edges. Simulations in any number of space dimensions will be facilitated and improved with a convenient package of plasma transport parameters, introduced here, that covers the NIC experiments discussed in this paper.

Mix is sensitive to transport parameters; a reasonably accurate determination of their values reduces model uncertainty. Remaining uncertainties concern a mixing model drag coefficient extrapolated beyond its presently validated limits to the highly variable and low Schmidt number ICF regime, and the influence of spherical geometry. Two-dimensional

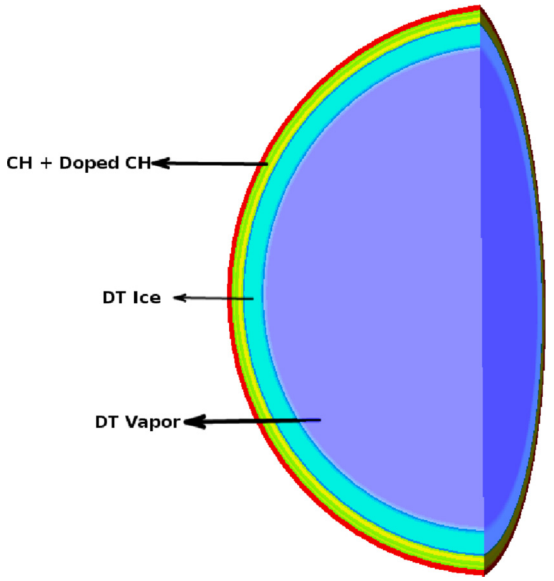

FIG. 1. The three principal layers of an ICF capsule.

simulations, independent of the mix model, provide a level of confirmation for our conclusions.

In Sec. II, we summarize aspects of the theory of mixing important for the present paper. In Sec. III we analyze the dimensionless Schmidt (Sc) and Prandtl (Pr) numbers,

$$\mathrm{Sc} = \frac{\text{viscous diffusivity}}{\text{concentration diffusivity}}; \quad \mathrm{Pr} = \frac{\text{viscous diffusivity}}{\text{thermal diffusivity}}. \tag{1}$$

These ionic-level transport parameters are major determinants of concentration and thermal mixing (whether due to turbulent or nonturbulent stirring) of the fluids.

In Sec. IV, we analyze 3D instabilities using 1D simulations. We start with a diffusion model applied to the RM instabilities (of unknown initial amplitude in our analysis, as we do not model the ablation phase of the implosion). If the diffusion (physical or numerical) is sufficiently strong, in combination with the initial amplitude perturbations, then the mixing crosses an RT stagnation instability threshold and becomes highly unstable. We confirm that this scenario cannot occur on the basis of physical mass diffusion, but it is possible through numerical diffusion based on Eulerian calculations for all but exceedingly fine grids. It is also possible due to combined effect instabilities with strong RM initial perturbations or for ablation-induced instabilities.

The 1D simulations, using the ICF codes HYDRA [2] and FLASH [3] pertain only to the fuel capsule, described in Refs. [4,5]. 2D simulations, given in Sec. V, support the mix analysis of Sec. IV. Conclusions are discussed in Sec. VI.

II. TRANSPORT AND MIX

The important scientific principles which govern mixing phenomena are—broadly speaking—transport, initial conditions, mode competition, dominant or single-mode growth rates, and multimode growth rates. In many cases, we see that parameters which characterize these phenomena are better understood for planar geometry mix, so extrapolation to mix in spherical geometry introduces uncertainty into the analysis.

A. Transport

We note the importance of fluid transport for the study of mix. Three important sources of transport are

(i) molecular or ionic (physically generated),

(ii) turbulent (numerically mesh generated from averages of nonlinear quantities), and

(iii) numerical (algorithmically generated).

Turbulent transport is based on subgrid scale models, according to a widely accepted dynamic theory [6–8]. It occurs neither in the governing Navier-Stokes equation nor in its solution at a direct numerical simulation (DNS) level of numerical resolution. It is needed for Reynolds-averaged Navier-Stokes (RANS) and large eddy simulation (LES). Numerical transport should be eliminated to the extent possible and in any case should be kept lower than the total transport, because diffusion, once added to a simulation, cannot be removed. The required numerical technology, front tracking, has been successfully used for fluid mixing problems and

TABLE I. Comparison of simulation to experiment, for the RT growth rate α. Discrepancy refers to the comparison of results outside of uncertainty intervals, if any, as reported. We omit simulations in gross disagreement with experiment and also those which achieve one parameter agreement with experiment through tuning one adjustable parameter. We acknowledge that there may be other validated, parameter-free RT simulations, of which we are unaware.

Ref.	Expt.	Sim. Ref.	α_{expt}	α_{sim}	Discrepancy
			LES/SGS/FT		
[12]	No. 112	[9]	0.052	0.055	6%
[12]	No. 105	[10]	0.072	0.076±0.004	0%
[12,13]	10 expt.	[11]	0.055–0.077	0.066	0%
[14]	air-He	[15]	0.065–0.07	0.069	0%
[16]	hot-cold	[9,10]	0.070±0.011	0.075	0%
[17]	salt-fresh	[10]	0.085±0.005	0.084	0%
			DNS		
[16]	hot-cold	[16]	0.070±0.011	∼0.070	0%
			Particle methods		
[18]		[18]		0.06±0.005	

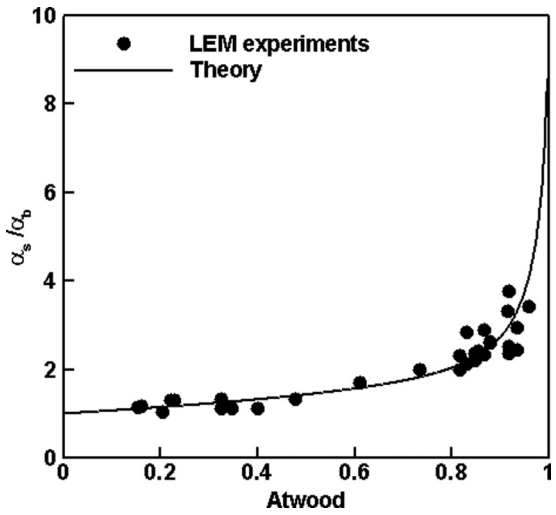

FIG. 2. The ratio of α_s/α_b as a function of Atwood number is shown for $\alpha_b \sim 0.05$. The solid dots are data from LEM experiments [33] and the solid curve is data from the model in Ref. [30].

is now available in the form of an application programing interface (API) for ease of insertion into physics codes. For use here, we have inserted it into FLASH.

In a series of papers [9–11], the authors and coworkers presented accurate simulation studies of the RT dimensionless mixing rates, validated against rocket rig and splitter plate experimental data,

$$\alpha = \text{mix penetration distance}/Agt^2, \tag{2}$$

with Atwood number A and acceleration g. See Table I.

We also mention some more detailed code comparisons. These include an RM comparison between the multiphysics code RAGE and FronTier (FT) [19], and comparison of converged LES–front tracking simulations [20] of the second moment of the velocity and other fluid variables that have been measured in a laboratory RT experiment.

Our previous work addressed convergence issues for probability density functions (PDF) and their indefinite integrals, the cumulative distribution functions (CDF) [21,22] with experimental validation in Refs. [20,23,24], relative to the hot-cold water splitter experiments [16]. We have also considered two-point statistical descriptions of RT and RM mixtures [25–27]. Simulation of second moments provides data for RANS simulations, but convergence criteria for second moments are more demanding of a simulation than are convergence criteria for mean quantities or overall mixing rates.

B. The buoyancy-drag equation

Our analysis of RT mix and mixing zone edges in Sec. IV is based on the variable acceleration buoyancy-drag equation [28–30],

$$(\rho_i + k_i\rho_{i'})\frac{dV_i}{dt} = (\rho_i - \rho_{i'})g(t) - (-1)^i\frac{C_i\rho_{i'}V_i^2}{|h_i|}, \quad i = 1,2, \tag{3}$$

where the "added mass" coefficient k_i, and the drag coefficient C_i, are the model's phenomenological parameters, $i = 1 = b$ (bubble) and $i = 2 = s$ (spike), and $V_i \equiv dh_i/dt$ is the velocity of the edge i of the mixing zone, with h_i the mixing zone height. Also A is the Atwood number, ρ_1 and ρ_2 are the light and heavy fluid densities, and $i' = i + 1(mod2)$ is the opposite index to i. This formula allows a unified treatment of bubble and spike growth rates for both Rayleigh-Taylor and Richtmyer-Meshkov instabilities [30]. Specifically the four parameters α_i, θ_i, $i = 1,2$ characterizing Rayleigh-Taylor and Richtmyer-Meshkov bubble and spike asymptotic growth rates are not independent. Any three are determined by specification of the fourth. We take the remaining single free parameter as the RT bubble growth rate, which is given by the bubble merger multimode growth rate as an independent theory [31] in agreement with experimental data.

The form of the drag force reflects the assumption that the fluid infinitely far upstream of the bubble or spike is stagnant. We consider cylindrical bubbles and spikes with $k_i \sim 1$ and the drag coefficient given by

$$C_i = \frac{1/\alpha_i - [1 + (-1)^i A] - k_i[1 - (-1)^i A]}{2[1 - (-1)^i A]}, \tag{4}$$

where α_i is the RT growth rate. For given α_b, the growth rate of spikes (α_s) can be obtained by assuming a stationary center of mass of the mixing layer [30]. The results, with the choice $k_i \sim 1$, are in good agreement with the linear electric motors (LEM) experiment data [30,32,33], as shown in Fig. 2 taken from Ref. [30], with additional validation data to be found in Ref. [30]. In using (3), we start at a specified location in the cold shell at the beginning of the deceleration phase. We refer to this point as the Lagrangian point. It is then followed with Lagrangian dynamics. Equation (3) yields equations for the associated RT bubble and spike tips. The acceleration is determined as a time derivative of the velocity interpolated to the Lagrangian point and the Atwood number is determined locally from the density variation over a region approximately bounding the bubble and spike tips.

We conclude that RT and RM instability growth rates are well understood, both theoretically and numerically (see Table I), but for planar geometry only. This knowledge is subsumed in the buoyancy-drag equation. As we apply this theory to determine the drag coefficient in the buoyancy-drag equation, we encounter extrapolation of the RT bubble growth rate beyond its validation range, a source of uncertainty for our analysis. The RM mixing stage is also RT stable (due to continued acceleration during the RM stage). The result is that the RM instabilities have no particular growth, and the instability growth during this period is modelled using concentration diffusion rather than a buoyancy-drag equation. The 2D simulations confirm the conclusions we draw.

III. TRANSPORT PARAMETERS

A. The transport package TICF

Fluid mixing depends on fluid transport. In this section we discuss ionic- or molecular-level transport in a plasma as a contributor to the total fluid transport. The plasma transport parameters depend sensitively on ablator and fuel equation of state properties. Our analysis indicates that physical transport has a quantifiable but not large effect on ICF simulations. We further note from Refs. [9,34] a 3% effect in the value of the

TABLE II. Transport models used to model CH vs. DT mixtures in an ICF capsule implosion.

Variable	Model	Γ	Θ	Summary
Viscous diffusion	Braginskii [47]	$\Gamma < 1$		Braginskii model for weakly coupled hot, diffusive plasmas
Viscous diffusion	Yukawa OCP [48]	$\Gamma > 1$	$0 < \Theta < 1$	Yukawa model for screened systems
Viscous diffusion	OCP [49]	$\Gamma > 1$	$\Theta \geqslant 1$	Model based on one component plasma
Mass diffusion	Chapman-Spitzer [50]	$\Gamma < 1$	$\Theta > 0$	Extends Chapman-Spitzer perturbation analysis with fit to screening
Mass diffusion	Cage [50]	$\Gamma > 1$	$\Theta > 0$	Yukawa one-component plasma model with screening
Thermal diffusion	Lee-More [51]			Classical thermal transport for ionized plasma

RT growth rate coefficient α from a factor of 2 modification in the transport. Accordingly, we emphasize a conveniently constructable transport package, rather than one of higher complexity, to include all latest improvements in plasma models.

Our models are calibrated to quantum molecular dynamics (QMD) data, as is our selection of the viscous and concentration diffusion models employed. A drawback of this calibration is the sparcity of QMD data in the warm dense matter regime. In the plasma transport package TICF (Transport For Inertial Confinement Fusion) we propose, the thermal conduction models are based on theory; the QMD-based approach could be adopted for them as well. The TICF models are sufficient for the hot-spot region of parameters, while their use in the earlier, outer, regions of the implosion would be ideally replaced by more accurate methods, based on density functional theory and molecular dynamics (DFT-MD) [35,36] and the still-more-expensive quantum Monte Carlo methods. The orbital-based Kohn-Sham (KS) functional theory DFT (KS-DFT) is usually limited to temperatures of 50 eV while the orbital-free (OF) version of these ideas, constructed in the Thomas-Fermi-Dirac (TFD) form [37] with the Dirac exchange substituted with a modern exchange-correlation functional form, will reach higher temperatures and densities, at which this simpler TFD form becomes accurate [38,39].

Recently, many equation-of-state (EOS) experiments and calculations have been carried for materials that are involved in the ICF implosion [40–42]. Different approaches have been taken for first-principles-based EOS calculations ranging from quantum molecular dynamics to path integral Monte Carlo. Specifically, CH material properties have been extensively studied both experimentally and theoretically. The Hugoniot of the CH has been measured from gas-gun experiments [43] and laser–x-ray experiments [44]. Using the experimental data, a first-principals equation-of-state model for CH was constructed [45].

As noted [46], the large hot-spot viscosity leads to a sharply reduced hot-spot Reynolds number. The Reynolds number, depending on velocity fluctuations, is estimated as 10^0–10^2 for the hot spot and 10^4–10^5 for the cold shell [46].

The same plasma properties affect the thermal conductivity and species concentration diffusivity, with the result that for the hot-spot Prandtl and Schmidt numbers Pr and Sc, $\mathrm{Pr} \leqslant \mathcal{O}(10^{-1})$ and $\mathcal{O}(10^{-1}) \leqslant \mathrm{Sc} \leqslant \mathcal{O}(1)$. The large variation in Sc is due to its dependence on the relative concentration χ of the CH and DT ions,

$$\chi = \frac{i_{\mathrm{CH}}}{i_{\mathrm{CH}} + i_{\mathrm{DT}}}, \tag{5}$$

where i_{CH} and i_{DT} are the respective ion number densities.

Both the viscosity and the species diffusion are strongly influenced by charge screening, which replaces the long-range Coulomb interaction with a short-range exponentially decaying interaction potential. The screening length depends on the density of electrons. This in turn is influenced by the species concentrations, as the DT has fewer electrons to ionize than does CH. In contrast, the (colder, denser) cold shell viscosity is smaller.

We introduce a package of molecular-level viscosity, concentration diffusion, and thermal transport parameters, summarized in Table II, and building on prior work [47–51] for the NIC parameter regime. The package is a composite of existing models and model switching criteria, with the switching criteria respecting the limits of model validity. The switching criteria are defined in terms of the degeneracy parameter Θ and the plasma parameter Γ introduced below. Our transport package TICF covers the entire domain relevant to ICF experiments. In this sense, it appears to go beyond other currently published transport packages [52]. It is available from the URL www.ams.sunysb.edu/TICF and has been installed into the FLASH code.

The degeneracy parameter Θ, the ratio of electron-to-Fermi energies, determines the plasma state, as a classical plasma ($\Theta > 1$) or degenerate plasma ($\Theta < 1$). Specifically,

$$\Theta = \frac{k_B T_{\mathrm{ele}}}{E_f}, \tag{6}$$

where E_f is the Fermi energy, k_B is the Boltzmann constant, and T_{ele} is the electron temperature.

The plasma parameter Γ is the ratio of (Coulomb) potential energy to plasma kinetic energy. It measures the strength of the electron-ion coupling within the plasma [53]. For $\Gamma < 1$ the plasma is weakly coupled and for $\Gamma > 1$ it is strongly coupled. Γ is defined as

$$\Gamma = \frac{Z^{*2} q_{\mathrm{ele}}^2}{a T_{\mathrm{ion}} k_B}, \tag{7}$$

where T_{ion} is the ion temperature, $Z^* q_{\mathrm{ele}}$ is the species charge, and

$$a = \left(\frac{3}{4\pi n_{\mathrm{ion}}}\right)^{\frac{1}{3}} \tag{8}$$

is the average interparticle distance. Here n_{ion} is the number density of the ions. The Coulomb potential, whose value at separation a is $Z^{*2} q_{\mathrm{ele}}^2 / a$, governs the interactions between the ions. We model the nonideal, strongly coupled plasma with one-component plasma– (OCP) and Yukawa one-component

plasma– (YOCP) based viscosity models. Screening is modeled by a Yukawa OCP, with a dimensionless inverse screening length [48]

$$\kappa = a\frac{\sqrt{4\pi Z^* n_{\rm ion} q_{\rm ele}^2}}{\sqrt{(k_B T_{\rm ele})^2 + \left(\frac{2}{3}E_f\right)^2}}, \tag{9}$$

dimensionalized in terms of the ionic radius a. The OCP is the limiting case of YOCP with an infinite screening length, $\kappa \to 0$. For the HYDRA simulation we are analyzing, $0 < \kappa < 4$.

If $\Theta \approx 1$ and $\Gamma \approx 1$, then the plasma describes warm dense matter. When the plasma is weakly coupled, $\Gamma < 1$, it can be described as an ideal gas because the potential energy of the electrons is small compared to the average plasma kinetic energy. In this regime, we rely on the Braginskii approximation [47] for the kinematic viscosity when the plasma is fully ionized. The viscosity of the $\Gamma > 1$ plasma is computed by either the Yukawa viscosity model or the Bastea model [49], with a transition point depending on the plasma degeneracy Θ. Since the YOCP-based viscosity model provides a fit for the liquid metal and warm dense matter regime, we use this only when $0 < \Theta < 1$. During the Richtmyer-Meshkov instability, the matter is characterized by warm dense properties. The pure OCP Bastea model does not incorporate degeneracy effects, is not mapped to any special physical regime, and is used when $\Theta > 1$.

Multicomponent transport models are required for mixtures. We regard CH and DT as single entities and apply mixture models to these entities. The ionization-level Z^* is computed using More's parametrization [54] of Thomas-Fermi pseudo-ionization. We use $A_{\rm CH}$, the average atomic weight of the C_2H_3 molecule as given in Ref. [55], to model the CH material. The effective ionization $Z_{\rm eff}$ for binary mixtures is computed using the binary ionic mixture model [56],

$$Z_{\rm eff}^2 = \langle Z^* \rangle_{\rm av}^{\frac{1}{3}} \langle Z^{*\frac{5}{3}} \rangle_{\rm av}, \tag{10}$$

where $\langle Z^{*p} \rangle_{\rm av} = x_1 Z_1^{*p} + x_2 Z_2^{*p}$ with x_i the number concentration and Z_i^* the Thomas-Fermi ionization associated with element i.

The Spitzer model [57] is widely used to model thermal conduction in plasmas. This model breaks down in the warm dense plasma regime because the Coulomb logarithm becomes negative there. Lee-More [51] improved the calculation for thermal conduction of a warm dense plasma by developing a first-order approximation to the Boltzmann equation.

The concentration diffusion model starts with the self-diffusion parameter of each species, from which the mutual diffusion parameter is derived [50,58]. When the plasma is weakly coupled, the species diffusion parameter is determined via the Chapman-Spitzer approximation. Otherwise, we use the Cage model. In both cases, the models presented in Refs. [50,58] are enhanced to include screening.

We model thermal conduction using the Lee-More model [51]. The CH vs. DT mixture depends on an average atomic weight. The model includes screening when computing the Coulomb forces and is also applicable when the plasma exhibits degeneracy and strong ion coupling effects. The viscous and mass diffusion properties of CH vs. DT mixtures are derived from molecular dynamics simulations [48–50]. Given the empirical nature of the model and the possible influence of not using a MD-based thermal conduction model, the present results can only be regarded as contributing to the scientific understanding of the method. RT instability growth rates are only weakly sensitive to uncertainty in the transport parameters.

B. Transport properties for NIC

In Figs. 3 and 4 we postprocess a 1D post-shot HYDRA simulation, described in Ref. [4], using our transport package. We show concentration and thermal diffusion parameters, Sc and Pr, respectively, which are of fundamental importance in understanding the extent or limits of RM and RT mixing. In the first of these figures, the concentration of CH is set to 0, while in the second it is set to 10%.

Sc and Pr show a strong dependence on the relative CH vs. DT concentration χ. See Fig. 5 and the Appendix. Taking

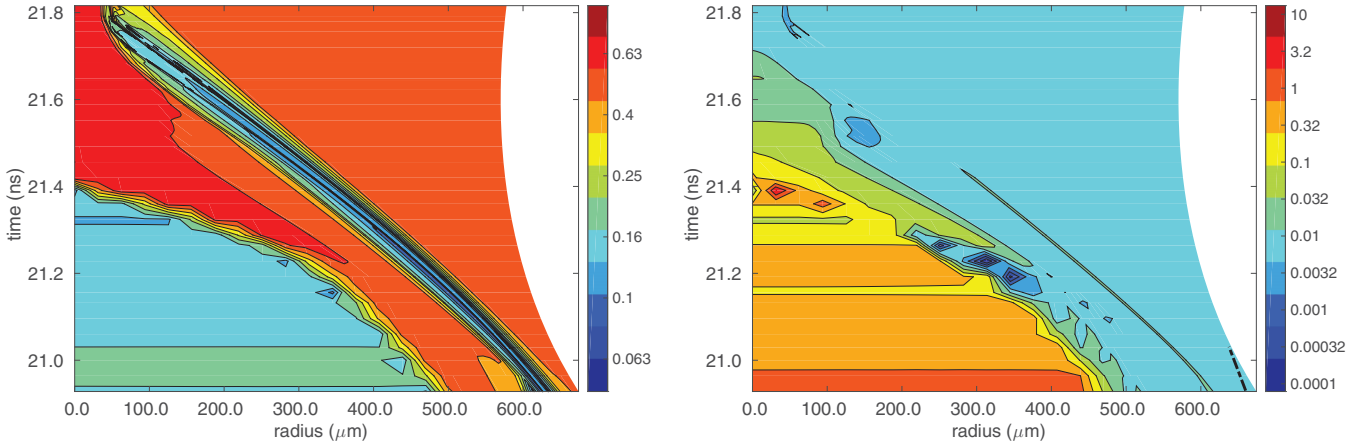

FIG. 3. RT phase of an ICF implosion in an r,t plot for the diffusion of the ablator into DT, Sc (left) and Pr (right) from a HYDRA simulation. From the left frame, we see that significant ablator into DT RT instabilities are allowed by the values of the transport parameters. From the right frame, we see that RT instabilities generated by thermally induced density gradients are regulated by the high levels of thermal conduction. The outer radius shown is outside the CH to DT interface.

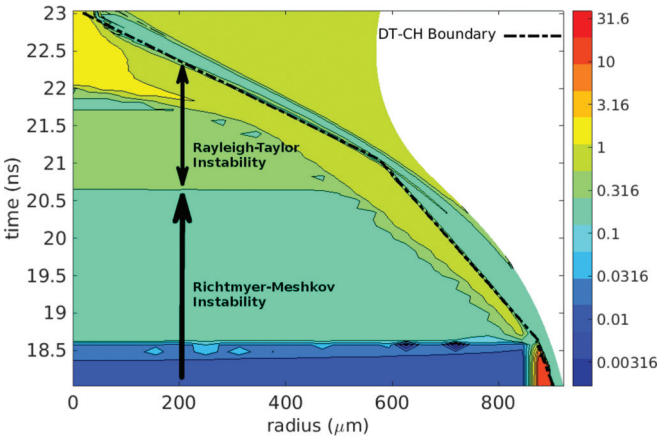

FIG. 4. Contour plot of Sc shown in the r,t space of a HYDRA simulation. The outer boundary of the plot includes approximately one-third of the ablator. The time (18 ns) starts shortly before the arrival of the fourth shock wave at the outer DT boundary. The black dashed line is the CH-DT boundary. The RM phase begins at 14.5 ns with the shock arrival at the CH-DT boundary (not shown in this figure). After the arrival of the fourth shock at this interface (18.5 ns), the CH-DT concentration χ becomes important. The plot assumes a 10% relative concentration of CH in the mixture and, at this value, Sc is large enough to allow significant DT-ablator mixing at both the RM and RT stages. If RM and RT spikes enter into the DT, diffusivity of the concentrations guarantees that all concentration values will occur as one passes through the spike from interior to exterior; 10% was chosen as an arbitrary value within this continuum of choices.

as typical hot-spot temperature and density $T = 4.5$ keV and $\rho = 63$ g/cm^3, we study Sc and Pr as functions of the relative CH vs. DT concentration χ. The dependence of these parameters on χ results from their large electron density in the CH-rich region, which accounts for an increase in the screening length, resulting in smaller Sc and Pr values, see Fig. 5. A similar concentration dependence occurs during the RM stage, see the Appendix. The nonmonotone dependence of Sc on concentration is not a consequence of switching between models. This region lies entirely within the scope of the Bastea model. It is rather a direct consequence of the Bastea OCP model itself, due to competing and opposite effects resulting from increased CH concentration. Among the multiple thermodynamics effects, we isolate what appear to be primary drivers. The increase in Sc for concentration in the interval [0.0,0.05] results from the increased proportion of heavy ions (which diffuse less rapidly). The decrease in Sc over the concentration interval [0.05,1], in contrast, is also driven by an increasing fraction of CH, which increases the electron density, thus increasing the screening length and lowering the viscosity. In any case, the screening effects of the plasma have a characteristic length scale of [0.3,0.6] Å in the hot spot, which implies that the hot-spot plasma is weakly screened and as a result the dimensionless transport parameters become independent of screening at bang time.

The variation of Sc has hydrodynamical, mixing, and possible numerical significance. The larger values of Sc at high DT concentration suggest a novel RT mixing behavior. The authors are not aware of scientific studies of mixing in which the concentration diffusivity and Schmidt number has such a striking dependence on the concentration. We suggest as a possible consequence that the RT spike and bubble will have well-defined outer boundaries but will still allow significant DT diffusion interior to the spike. We would suggest an RT bubble growth rate of perhaps $\alpha = 0.06$, in lieu of more detailed scientific analysis, not presently available, and with α spike values coming from the theoretical relations of Ref. [30]. For less than DNS resolution, the values of Sc also suggest a role for a front tracking simulation [20,59] to avoid excess numerical concentration diffusion.

In dense plasmas, free electrons orbit in close vicinity of ions. Therefore, the ions are no longer isolated. The screening induced from the dense environment skews their atomic energy levels, which in turn causes ionization potential depression (IPD). IPD is a key factor for understanding the ionization balance, charge state distribution, opacity, and plasma equation of state. IPD occurs when a neighboring charged particle disrupts the ionic potential of an ion immersed in a plasma. IPD can be seen in two limits, the Debye shielding model

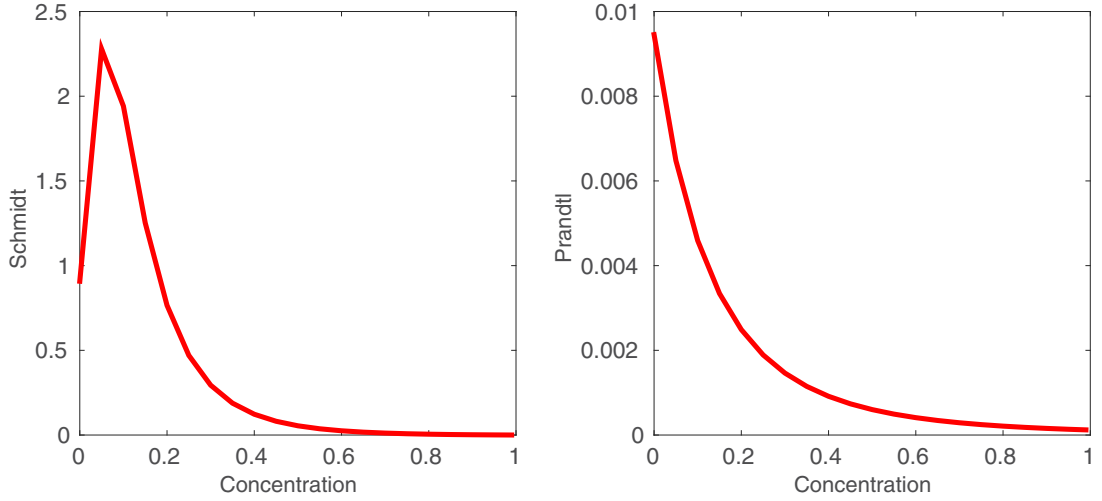

FIG. 5. The range Sc and Pr values as the concentration $\chi = \frac{i_{CH}}{i_{CH}+i_{DT}}$ is varied for fixed $T = 4.5$ keV and $\rho = 63$ g/cm^3, typical values for the hot spot at bang time.

and the ion sphere model (IS). The Debye shielding model holds when the plasma is in a weakly coupled regime, where the Debye length is greater than the interparticle spacing. In high-energy-density (HED) plasmas, the number of particles in a Debye sphere are considerably lower, and instead we use the ion sphere model.

The IPD has been formulated in two ways. Stewart and Pyatt (SP) [60] solve for the IPD by calculating the electrostatic potential of the charged particles within the framework of the Thomas-Fermi theory. Ecker-Kroll (EK) [61] developed a generalized form of the Saha equation, based on the plasma chemical potential.

The SP and IS models are favored over the EK models in Orion laser experiments [62], but the reverse is true for experiments at the Linac Coherent Light Source [63]. The experiments show that the IPD depends on the temperature and density, which different between the two experiments, but a detailed analysis of the discrepancy is still lacking. We believe that the IPD for our ICF simulation falls somewhere in between the SP and EK models with the choice treated as domain specific.

IV. MIX MODELS AND MIXING ZONE EDGES

We state our main results in this section, based on 1D simulations augmented by a buoyancy-drag mix model and confirmed by 2D simulations in Sec. V. We find the following:

(1) There is only a minor effect from concentration diffusion into the hot spot or the cold shell from the cold shell-gas T vs. D concentration discontinuity, or from the DT to CH boundary, based on the RM and RT stages of the implosion; see Fig. 6.

(2) Untracked Eulerian simulations, at the resolution level of a finely gridded 3D simulation, show significant numerical effects, crossing an RT instability threshold, resulting in significant mixing of CH into DT in the cold shell. The effect is eliminated by Eulerian mesh refinement, by Lagrangian simulation codes, or by front tracking. The effect serves as a caution for the use of Eulerian codes for implosion problems. In the present context, approx 5000 cells (0.25-micron resolution) in the radial direction are needed to remove the numerical aspects of the simulation and to obtain a converged solution, with even qualitative agreement with the Lagrangian (HYDRA) or front tracking solutions. See Fig. 7. At higher levels of numerical diffusion, RM initial amplitudes, or ablation-induced instabilities, an effect on the hot-spot thermal properties is possible. See Sec. V.

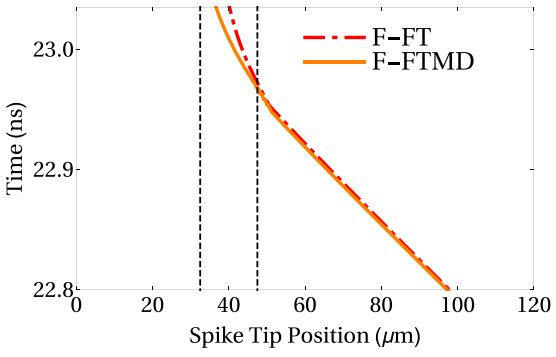

FIG. 6. We plot the inner radius of the CH spikes in r,t space of an NIC implosion for FLASH-tracked simulations with (F-FTMD) and without (F-FT) physical mass diffusion. The spike tip location is assessed from the buoyancy-drag equation associated with the 10% contour of CH. Only a minor effect from the addition of physical mass diffusion is observed at bang time, ≈23 ns. The inner and outer edges of the cold shell at bang time are demarcated on the plot with dashed vertical lines.

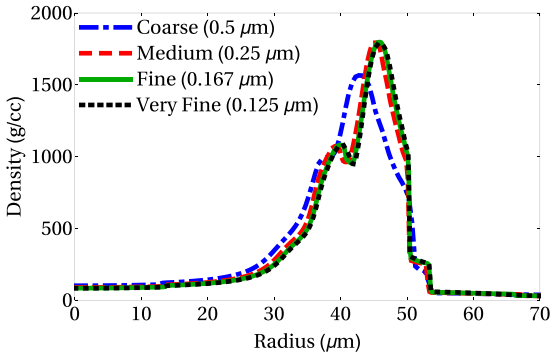

FIG. 7. A mesh convergence study for an untracked Eulerian simulation, showing density vs. radius at bang time. The nonconverged solutions have incorrect thermodynamics within the cold shell, see Sec. V, Fig. 8, but do not impact the hot-spot thermodynamics.

(3) Combined effects of amplitude growth at the initial gas to ice boundary and the RT unstable thermal gradient at the edge of the hot spot adds a mix-related component to the thermal diffusion, thereby reducing the size of the high temperature hot spot. See Sec. V.

(4) Combined effect of ablation and RT instabilities appear to be a possible cause of CH mix into the hot spot. See Sec. V.

To establish these points, we conduct comparison 1D simulations, and repeated in 2D, in Sec. V. To assess the effects of numerical concentration diffusion, we simulate with and without front tracking, with various levels of (1D) mesh refinement and with and without physical concentration diffusion.

The ICF instabilities start at the ablation surface, with a modified RT instability, due to drive asymmetries and surface imperfections. Next in time are the cold shell RM instabilities associated with each of the ablator-to-DT ice and DT ice–to–DT vapor interfaces. In the case of "low-foot" or NIC shots, these instabilities are driven by each of four shock waves. We omit until later discussion of the ablation instabilities that feed through to the RM initial amplitudes. Consequently, we set the RM initial conditions to those as measured on manufactured capsules. The importance of these is diminished by the nature of the RM evolution, which is in an RT stable (instability decreasing) regime. Thus we base our analysis of the RM phase not on the RM instabilities but on diffusive transport occurring within this period.

Following the RM phase in time is the RT stagnation instability. The locus of RT instability, set by outgoing pressure waves reflected from the origin, is close to the unperturbed DT-to-CH boundary.

To establish point (1), we consider the inner radius of the spikes of CH in 1D simulations augmented by the

buoyancy-drag mix model. We compare front-tracked solutions in Fig. 6, showing the CH spike penetration in r,t space. The minor change between the two tracked solutions at bang time, ≈23 ns (having no numerical CH concentration diffusion), with and without physical diffusion, shows the lack of importance of physical mass diffusion for NIC studies. To establish (2), we present a mesh refinement study in Fig. 7, plotting density vs. radius at bang time, with the medium mesh (0.25 μm) needed to reach a nearly converged solution for the thermodynamics. Significant temperature differences arise from CH diffusion into the hot spot, especially in the presence of strong RM initial conditions, see Fig. 9.

V. 2D SIMULATIONS

The purpose of this section is to confirm claims (1) and (2) of Sec. IV, to establish claim (3), and to discuss the basis for statement (4).

Using the University of Chicago High Energy Density Physics code FLASH [3], we conduct 2D capsule-only simulations of NIC campaign shot N120321. As FLASH does not have as sophisticated a laser deposition and ablation package as HYDRA, we use the data from the 1D HYDRA run to initialize FLASH at 14.5 ns, about 500 ps before the first shock hits the fuel to ablator interface. A more complete analysis of these 2D simulations can be found in Ref. [64].

A. Absence of hot-spot mix from instabilities arising at the DT-to-CH interface during the RT and RM implosion phases

We seed initial perturbations randomly into the fuel-to-ablator interface using spherical harmonics from mode 8 to 30, chosen to reflect the level of mesh resolution afforded in this study. These 2D simulations are designed to confirm the 1D simulations of Sec. IV. The initial rms amplitudes of the perturbations are chosen as 1 μm for the DT to CH interface and 1 μm (nominal) and 5 μm (strong) as a sensitivity study at the ice-to-gas interface.

The simulations show little growth of instability amplitude during the RM implosion stage due to the RT stable nature of this implosion stage. During the RT stage, enhanced growth is observed in the strong initial perturbation case, but not sufficient enough to cause CH spikes to penetrate into the hot spot using the front-tracked solution as a surrogate to the converged solution at bang time. See Fig. 8 bottom row, which shows both the nominal initial perturbation (left) and strong perturbation (right) CH concentrations that do not reach the hot spot. However, the combined effects of the coupling between the nearby perturbations at the initial ice-to-gas interface and steep thermal gradients at the edge of the hot spot predict a significant change in the hot-spot thermodynamics; see Fig. 9 of Sec. VC.

B. Numerically induced RT and RM mixing

We find a potential for a significant level of numerically induced mix in the cold shell for untracked Eulerian simulations with less than extremely refined grids. Comparing down the columns in Fig. 8, we show simulations with identical initial conditions, run at a resolution of 0.5 μm using an untracked Eulerian configuration (top) and tracked Eulerian (bottom). The numerical diffusion present in the untracked simulations is amplified when the level of instability increases in the stronger initial perturbation (right column). The level of single-effect RT or RM mixing is not sufficient to impact the hot-spot thermodynamics, but combined effects are considered in Sec. V C.

C. Combined effects, gas-to-ice, and thermal gradient RT instabilities

We observe a sensitivity to hot-spot thermodynamics from a coupling effect between stronger perturbations at the ice-to-gas boundary and the strong thermal gradients at the hot-spot edge. In Fig. 9, we show the hot-spot density via the color plot and temperature contours (2 keV and 5 keV moving inward) for the nominal perturbation (left) and strong perturbation (right). The top half of each figure represents the 2D solution, which can be compared to the 1D solution in the bottom half of each frame. Both simulations are front-tracked Eulerian, as representative of a converged solution, but only a minor sensitivity was observed between the front-tracked and untracked solutions for the hot-spot thermodynamics. The enhanced mixing reduces the temperature in the central hot spot with no 5-keV contour present in the right frame.

D. Combined effects: Ablation and DT-to-CH RT instabilities

According to post-shot NIC simulations, 200 ng (N120321) [65] or 50 ng (N120321) [66] of CH is premixed into the hot spot to capture the effects of ablator mix in the hot spot observed in the experiments, independent of the effects generated by the tent and fill tube [65]. Here we address the question of a physics-based mechanism for this mix to occur.

Mode 2 instabilities of magnitude 8.3% and 15% have been reported for shots N120321 and N120215 [67,68]. The amplitude of mode number 6 and higher instabilities are not measured. The time-dependent locus of RT instability (reversal of the direction of acceleration from inward to outward) lies inside the cold shell and is near the CH boundary at the late implosion stages, with a radius beginning at ≈30% of the CH inner boundary radius at the onset of the deceleration stage. As the deceleration phase progresses, this RT instability locus moves towards the CH boundary as the pressure equilibrates from the outward moving stagnation shock. In Fig. 10 (left), we plot the inner radius of the CH spike tips, as predicted by the 1D mix model analysis of a simulation started at the beginning of the RT deceleration phase. We show a range of perturbation amplitudes, measured as a fraction of the unperturbed CH radius. If the amplitude exceeds 10–15% of the DT radius at the initiation time for the RT instability, we observe spike tips penetrating into the hot spot.

To justify the use of the buoyancy-drag model for predictions of the CH spike penetration, in Fig. 10 (right), we compare the predicted 3D mix from the model against the observed spike penetration from a companion 2D simulation. The simulation used for this comparison was the FLASH base simulation with a strong initial perturbation run from the beginning of the RM phase. The early increased amplitude in the simulation (solid blue line) is a result of the extra vorticity

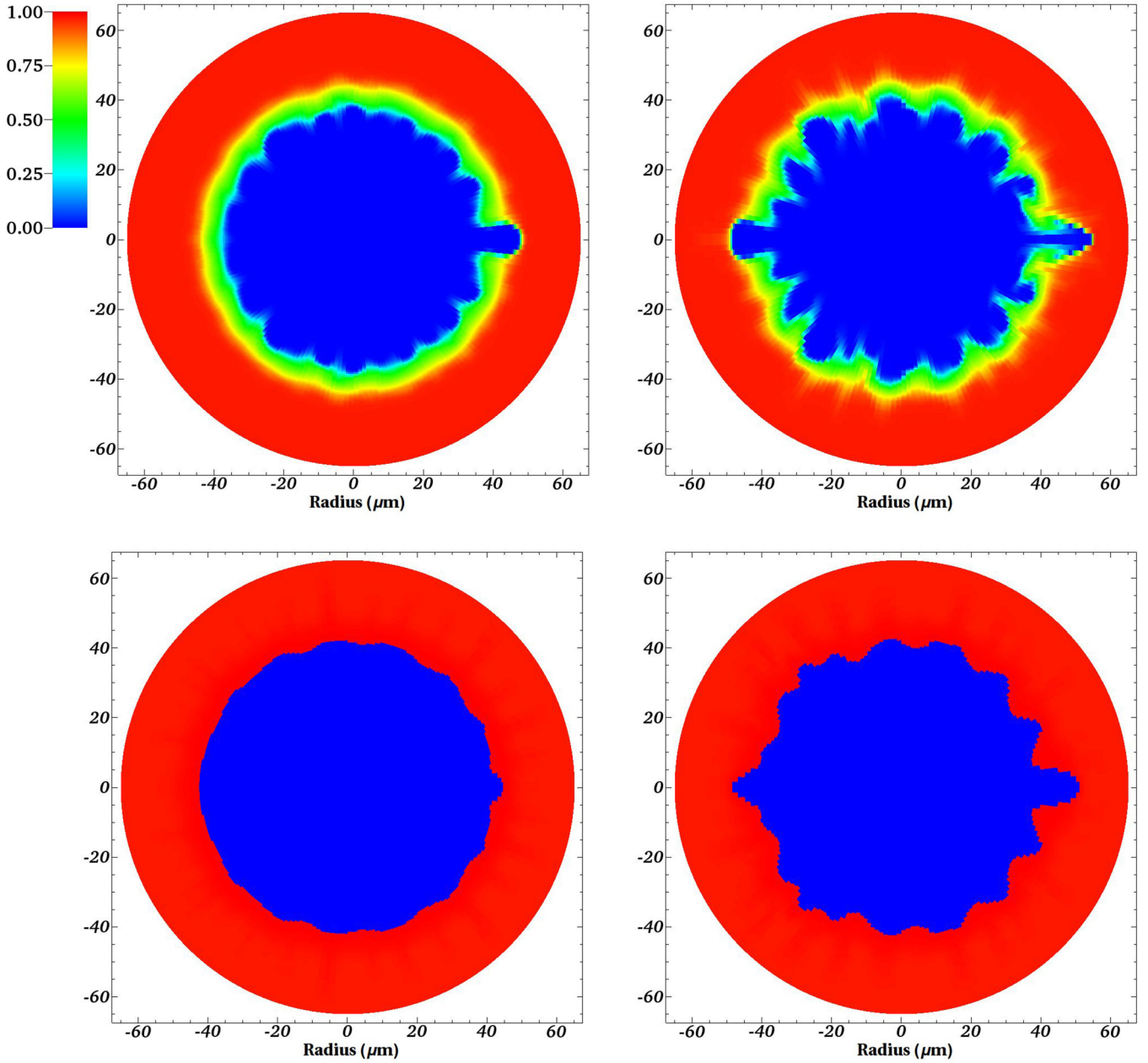

FIG. 8. CH spike edges at bang time for both nominal (left) and strong (right) RM initial conditions. When compared, the top row (without front tracking) and bottom row (with front tracking) show a large impact on the CH penetration due to numerical diffusion which interacts with the RT instability and is pulled inward. When comparing the nominal and strong initial conditions, a coupling effect between the larger perturbations and the growth of the instability at the thermal gradient, where the main potential for mixing occurs, is observed.

in the solution from the increased size of the perturbation, which is not present in a 1D model. As bang time is approached (23.1 ns for this simulation), the buoyancy-drag model slightly overpredicts the growth allowing the lines to converge. Overall, the buoyancy-drag model has reasonably good agreement with the 2D spike penetration. This suggests that the model should be a reasonable predictor of 3D mix and can be used for parameter studies based off of 1D simulations.

Based on the spike penetration observed for various perturbation amplitudes, it is possible that an ablation driven instability can push the CH across this critical RT unstable locus and onto a trajectory of inward-directed spike development. Such an event is consistent with the experiments and analysis of Ref. [69], and, moreover, we have a quantitative estimate of the amplitude needed to generate the instability, see Fig. 10 (left). Current NIC simulations [70] focus on localized defects on the ablator outer surface as generating narrow CH spikes, which presumably couple to the RT unstable point, as analyzed in Fig. 10. See also the related experimental work in Ref. [71].

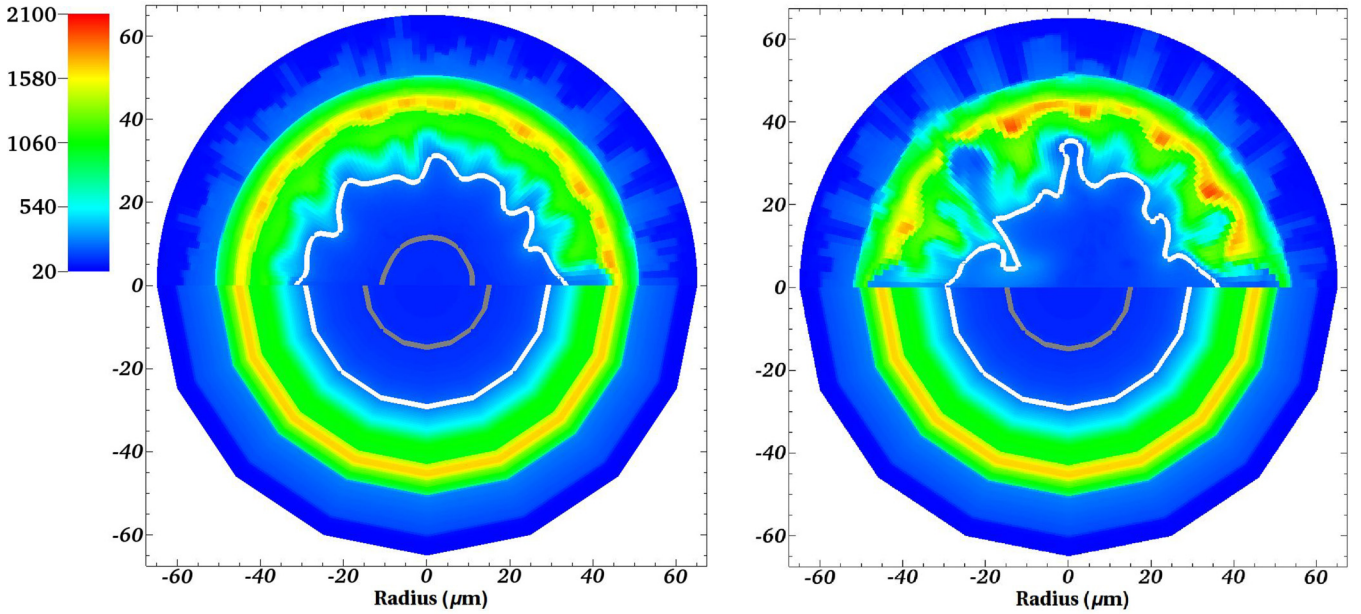

FIG. 9. Thermodynamics of the hot spot at bang time as observed through the density plots (color) and temperature contours (moving inwards 2-keV and 5-keV levels). Left: Front-tracked Eulerian nominal initial perturbation. Right: Front-tracked Eulerian strong initial perturbation. The top half of each frame is the 2D simulation compared with the bottom half from the companion 1D simulation. Enhanced mixing induced by the stronger initial perturbation results in the complete elimination of the 5-keV contour and thus a lowering of the hot-spot temperature, degrading the performance of the capsule.

VI. DISCUSSION

Our proposed model indicates that the NIC design is located near a performance cliff, a conclusion consistent with NIF and NIC experimental data. We find no single mechanism mix-related effects from the RM and RT implosion stages but possible effects from combined mechanisms.

We find at most marginal effects from mass (CH-DT or D-T concentration) diffusion but possible combined RM and RT mix-related effects on the hot-spot thermodynamics.

We find significant effects from numerical mass diffusion for Eulerian codes for all but the most extreme levels of mesh refinement. These effects are associated with the CH-DT interface and have a possible (numerically induced) impact on the hot-spot thermodynamics.

We discuss an ablation-RT combined effect which may lead to CH mix in the hot spot.

The basis for these results is a 1D mix model simulation for NIC experiments, based on buoyancy-drag equations. This equation together with its parameters have been extensively validated but are used here outside of the validation regime, and for this purpose we propose estimates based on judgment and available knowledge. Additionally, the equation and its validation have been carried out for planar but not spherical geometry. Uncertainties in the mix model, as applied to NIC,

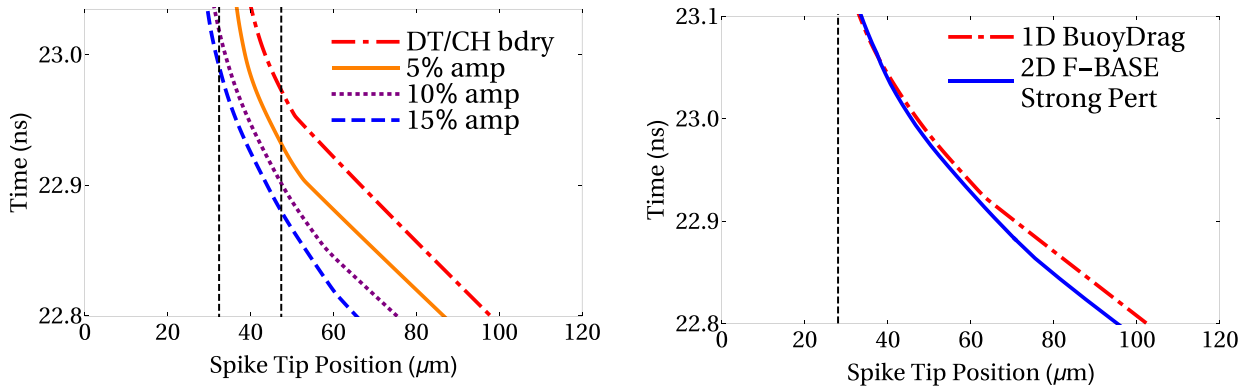

FIG. 10. Left: Penetration of the CH spike tips into the DT fuel at bang time, in an r,t plot, for a range of perturbation amplitudes, using a simulation initialized at the beginning of the RT stage. For amplitudes in excess of 10–15%, we observe penetration of spikes into the hot spot. The dotted black lines represent the edge of the hot spot and cold shell region at bang time (≈23 ns), respectively. Right: Comparison of 1D buoyancy-drag model against 2D spike penetration from companion simulation initialized at the beginning of the RM stage. Reasonable agreement is observed between the buoyancy-drag model and the simulated spike penetration through bang time (≈23.1 ns), suggesting that the model can be used for prediction of 3D mix.

include RM initial conditions, extrapolation of the model drag coefficient beyond their presently validated limits, and the effects of spherical geometry.

Two-dimensional simulations are conducted using FLASH and with front tracking added via an API for convenience of code development. The 2D simulations confirm the 1D and mix model analysis of Sec. IV. Additionally, they identify combined effect mixing instabilities not identified by the 1D analysis. Specifically, we find coupling between instabilities at the ice-to-gas boundary and the RT stagnation instability, which lowers the hot-spot temperature even without introducing CH into the hot spot.

In support of the mix model and the 2D simulations, we have determined parameterized plasma transport models, with model switching criteria, showing significant variation as the implosion progresses. The transport package is available to others and could aid future HED simulation studies.

ACKNOWLEDGMENTS

This manuscript has been coauthored by Los Alamos National Laboratory, under Contract No. JL3K00 NYSB0000, Inertial Confinement Fusion Campaign, Los Alamos preprint LA-UR 16-20021. This research used resources of the National

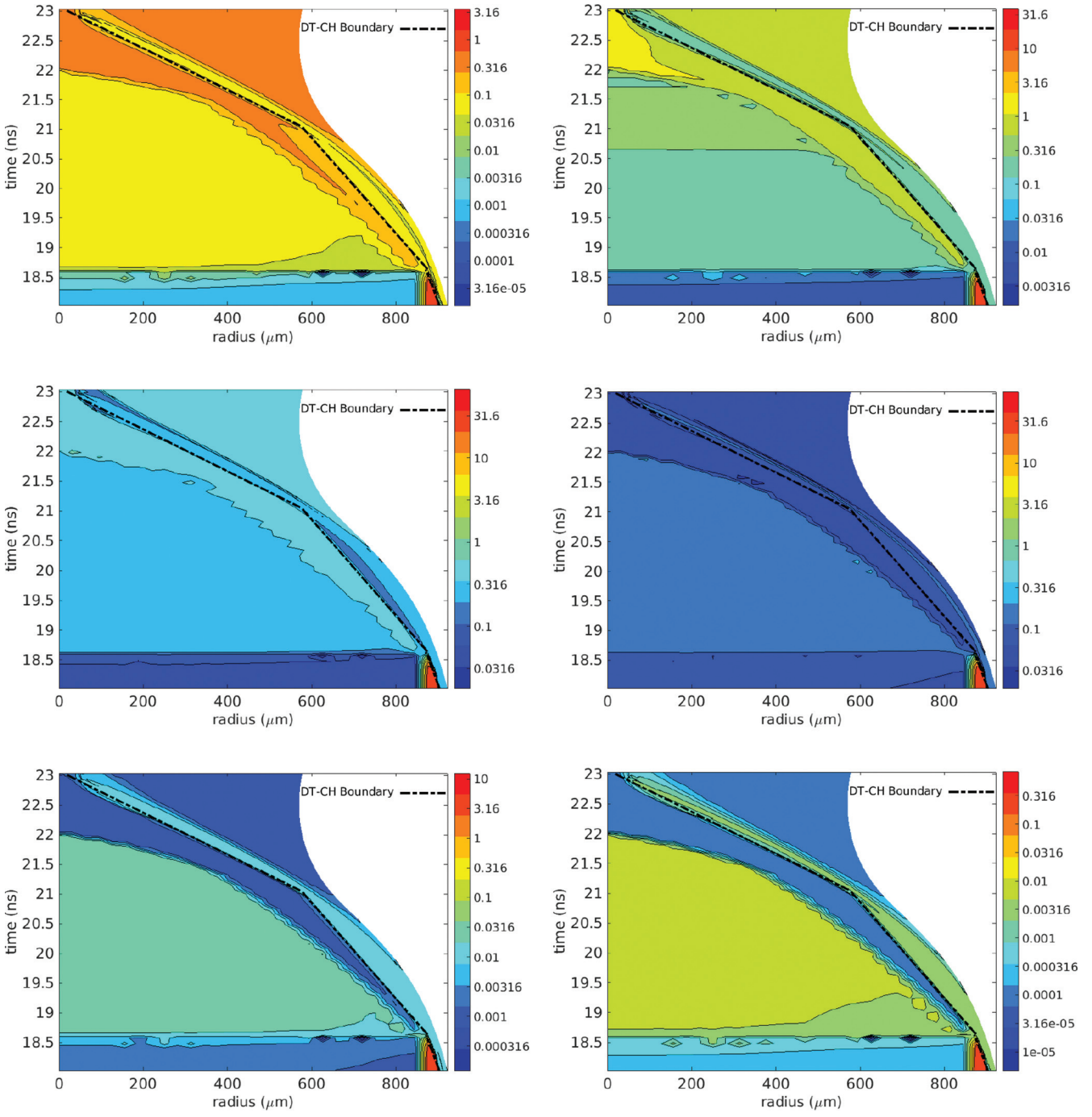

FIG. 11. The Schmidt number in the radius, time space of a NIC implosion, for a representative sequence of CH-DT relative concentrations.

Energy Research Scientific Computing Center, which is supported by the Office of Science of the U.S. Department of Energy under Contract No. DF-AC02005CH11231. This research used computational resources of Lawrence Livermore National Laboratory. It is a pleasure to thank Lee Collins and Joel Kress for helpful comments.

APPENDIX: CONCENTRATION-DEPENDENT RM AND RT SCHMIDT NUMBERS

In Fig. 11, we plot Schmidt number in the r,t space of a NIC implosion for a representative sequence of CH-DT relative concentrations.

[1] D. S. Clark, C. R. Weber, J. L. Milovich, J. D. Salmonson, A. L. Kritcher, S. W. Haan, B. A. Hammel, D. E. Hinkel, O. A. Hurricane, O. S. Jones, M. M. Marinak, P. K. Patel, H. F. Robey, S. M. Sepke, and M. J. Edwards, Phys. Plasmas **23**, 056302 (2016).
[2] M. M. Marinak, G. D. Kerbel, N. A. Gentile, O. Jones, D. Munro, S. Pollaine, T. R. Dittrich, and S. W. Haan, Phys. Plasmas **8**, 2275 (2001).
[3] B. Fryxell, K. Olson, P. Ricker, F. X. Timmes, M. Zingale, D. Q. Lamb, P. MacNeice, R. Rosner, J. W. Truran, and H. Tufo, Astrophys. J. Suppl. **131**, 273 (2000).
[4] J. Melvin, H. Lim, V. Rana, B. Cheng, J. Glimm, D. H. Sharp, and D. C. Wilson, Phys. Plasmas **22**, 022708 (2015).
[5] J. Melvin, H. Lim, V. Rana, B. Cheng, J. Glimm, D. H. Sharp, and D. C. Wilson, J. Phys. Sci. Appl. **5**, 24 (2015).
[6] A. Honein and P. Moin, Numerical aspects of compressible turbulence simulations, Report No. TF-92, Stanford University, 2005.
[7] P. Moin, K. Squires, W. Cabot, and S. Lee, Phys. Fluids A **3**, 2746 (1991).
[8] U. Piomelli, W. H. Cabor, P. Moin, and S. Lee, Phys. Fluids A **3**, 1766 (1991).
[9] H. Lim, J. Iwerks, J. Glimm, and D. H. Sharp, Proc. Natl. Acad. Sci. USA **107**, 12786 (2010).
[10] J. Glimm, D. H. Sharp, T. Kaman, and H. Lim, Philos. Trans. R. Soc. London A **371**, 20120183 (2013).
[11] E. George, J. Glimm, X.-L. Li, Y.-H. Li, and X.-F. Liu, Phys. Rev. E **73**, 016304 (2006).
[12] V. S. Smeeton and D. L. Youngs, Experimental investigation of turbulent mixing by Rayleigh-Taylor instability (part 3), AWE Report Number 0 35/87 (1987).
[13] K. I. Read, Physica D **12**, 45 (1984).
[14] P. Ramaprabhu and M. Andrews, J. Fluid Mech. **502**, 233 (2004).
[15] X.-F. Liu, E. George, W. Bo, and J. Glimm, Phys. Rev. E **73**, 056301 (2006).
[16] N. Mueschke and O. Schilling, Phys. Fluids **21**, 014106 (2009).
[17] N. J. Mueschke, Experimental and Numerical Study of Molecular Mixing Dynamics in Rayleigh-Taylor Unstable Flows, Ph.D. thesis, Texas A&M University, 2008.
[18] K. Kadau, T. C. Germann, N. G. Hadjiconstantinou, P. S. Lomdahl, G. Dimonte, B. L. Holian, and B. J. Alder, Proc. Natl. Acad. Sci. USA **101**, 5851 (2004).
[19] T. O. Masser, The Effects of Temperature Equilibrium in Mixed Cell Hydrodynamics, Ph.D. thesis, State University of New York at Stony Brook, 2007.
[20] J. Glimm, H. Lim, W. Hu, B. Plohr, and D. H. Sharp, Ann. Math. Sci. Appl. **1**, 149 (2016).
[21] T. Kaman, R. Kaufman, J. Glimm, and D. H. Sharp, in *Uncertainty Quantification in Scientific Computing*, IFIP Advances in Information and Communication Technology, edited by A. Dienstfrey and R. Boisvert (Springer, Berlin, 2012), Vol. 377, pp. 212–225.
[22] J. Melvin, P. Rao, R. Kaufman, H. Lim, Y. Yu, J. Glimm, and D. H. Sharp, High Energy Density Phys. **9**, 288 (2013).
[23] P. Rao, J. Melvin, W. Hu, R. Kaufman, H. Lim, and J. Glimm, in *11th World Congress on Computational Mechanics (WCCM XI)* (2014).
[24] J. Glimm, D. H. Sharp, H. Lim, R. Kaufman, and W. Hu, Philos. Trans. R. Soc. London A **373**, 20140282 (2015).
[25] J. Glimm, J. W. Grove, X.-L. Li, W. Oh, and D. H. Sharp, J. Comput. Phys. **169**, 652 (2001).
[26] H. Lim, Y. Yu, J. Glimm, X. L. Li, and D. H. Sharp, Phys. Scr. **T142**, 014062 (2010).
[27] H. Lim, Y. Yu, H. Jin, D. Kim, H. Lee, J. Glimm, X.-L. Li, and D. H. Sharp, Comput. Methods Appl. Mech. Eng. **197**, 3435 (2008).
[28] G. Dimonte and M. Schneider, Phys. Fluids **12**, 304 (2000).
[29] D. Oron, O. Sadot, Y. Srebro, A. Rikanti, Y. Yedvab, U. Alon, L. Erez, G. Erez, G. Ben-Dor, L. A. Levin, D. Ofer, and D. Shvarts, Lasers Part. Beams **17**, 465 (1999).
[30] B. Cheng, J. Glimm, and D. H. Sharp, Phys. Lett. A **268**, 366 (2000).
[31] B. Cheng, J. Glimm, and D. H. Sharp, Chaos **12**, 267 (2002).
[32] G. Dimonte and M. Schneider, Phys. Rev. E **54**, 3740 (1996).
[33] G. Dimonte, Phys. Plasmas **6**, 2009 (1999).
[34] H. Lim, J. Iwerks, Y. Yu, J. Glimm, and D. H. Sharp, Phys. Scr. **T142**, 014014 (2010).
[35] D. Hohl, V. Natoli, D. M. Ceperley, and R. M. Martin, Phys. Rev. Lett. **71**, 541 (1993).
[36] I. Kwon, L. A. Collins, J. D. Kress, N. Troullier, and D. L. Lynch, Phys. Rev. E **49**, R4771(R) (1994).
[37] F. Lambert, J. Clerouin, and G. Zerah, Phys. Rev. E **73**, 016403 (2006).
[38] L. Burakovsky, C. Ticknor, J. D. Kress, L. A. Collins, and F. Lambert, Phys. Rev. E **87**, 023104 (2013).
[39] S. X. Hu, L. A. Collins, V. N. Goncharov, J. D. Kress, T. R. Boehly, R. Epstein, R. L. McCrory, and S. Skupsky, J. Phys. **717**, 012064 (2015).
[40] J. Clérouin and J.-F. Dufrêche, Phys. Rev. E **64**, 066406 (2001).
[41] S. X. Hu, B. Militzer, V. N. Goncharov, and S. Skupsky, Phys. Rev. B **84**, 224109 (2011).
[42] M. A. Morales, L. X. Benedict, D. S. Clark, E. Schwegler, I. Tamblyn, S. A. Bonev, A. A. Correa, and S. W. Haan, High Energy Density Phys. **8**, 5 (2012).
[43] S. Marsh, *LASL Shock Hugoniot Data* (University of California Press, Berkeley, 1980).
[44] M. Koenig, F. Philippe, A. Benuzzi-Mounaix, D. Batani, M. Tomasini, E. Henry, and T. Hall, Phys. Plasmas, 3026 (2003).
[45] S. X. H., L. A. Collins, V. N. Goncharov, J. D. Kress, R. L. McCrory, and S. Skupsky, Phys. Plasmas, 043105 (2016).

[46] C. R. Weber, D. S. Clark, A. W. Cook, L. E. Busby, and H. F. Robey, Phys. Rev. E **89**, 053106 (2014).
[47] H. F. Robey, Phys. Plasmas **11**, 4123 (2004).
[48] M. S. Murillo, High Energy Density Phys. **4**, 49 (2008).
[49] S. Bastea, Phys. Rev. E **71**, 056405 (2005).
[50] J. Daligault, Phys. Rev. E **86**, 047401 (2012).
[51] Y. T. Lee and R. M. More, Phys. Fluids **27**, 1273 (1984).
[52] E. L. Vold, A. S. Joglekar, M. I. Ortega, R. Moll, D. Fenn, and K. Molvig, Phys. Plasmas **22**, 112708 (2015).
[53] D. Salzmann, *Atomic Physics in Hot Plasmas* (Oxford University Press, Oxford, 1998).
[54] R. More, Adv. Atom. Mol. Phys. **21**, 305 (1985).
[55] F. Lambert and V. Recoules, Phys. Rev. E **86**, 026405 (2012).
[56] J. P. Hansen, G. M. Torrie, and P. Vieillefosse, Phys. Rev. A **16**, 2153 (1977).
[57] L. Spitzer, *Physics of Fully Ionized Gases*, 2nd ed. (Interscience, New York, 1962).
[58] J. Daligault, Phys. Rev. Lett. **108**, 225004 (2012).
[59] R. Kaufman, H. Lim, and J. Glimm, Bull. Inst. Math. Acad. Sin. New Ser. **11**, 115 (2016).
[60] J. C. Stewart, J. Pyatt, and D. Kedar, Astrophys. J. **144**, 1203 (1966).
[61] G. Ecker and W. Kröll, Phys. Fluids **6**, 62 (1963).
[62] D. J. Hoarty, P. Allan, S. F. James, C. R. D. Brown, L. M. R. Hobbs, M. P. Hill, J. W. O. Harris, J. Morton, M. G. Brookes, R. Shepherd, J. Dunn, H. Chen, E. Von Marley, P. Beiersdorfer, H. K. Chung, R. W. Lee, G. Brown, and J. Emig, Phys. Rev. Lett. **110**, 265003 (2013).
[63] O. Ciricosta, S. M. Vinko, H.-K. Chung, B.-I. Cho, C. R. D. Brown, T. Burian, J. Chalupský, K. Engelhorn, R. W. Falcone, C. Graves, V. Hájková, A. Higginbotham, L. Juha, J. Krzywinski, H. J. Lee, M. Messerschmidt, C. D. Murphy, Y. Ping, D. S. Rackstraw, A. Scherz, W. Schlotter, S. Toleikis, J. J. Turner, L. Vysin, T. Wang, B. Wu, U. Zastrau, D. Zhu, R. W. Lee, P. Heimann, B. Nagler, and J. S. Wark, Phys. Rev. Lett. **109**, 065002 (2012).
[64] J. Melvin, Numerical Modeling of Hydrodynamic Instabilities and Their Impact on Mix in Inertial Confinement Fusion, Ph.D. thesis, Stony Brook University, 2016.
[65] D. S. Clark, M. M. Marinak, C. R. Weber, D. C. Eder, S. W. Haan, B. A. Hammel, D. E. Hinkel, O. S. Jones, J. L. Milovich, P. K. Patel, H. F. Robey, J. D. Salmonson, S. M. Sepke, and C. A. Thomas, Phys. Plasmas **22**, 022703 (2015).
[66] D. S. Clark, C. R. Weber, J. L. Milovich, J. D. Salmonson, A. L. K. andS. W. Haan, B. A. Hammel, O. A. Hurricane, O. S. Jones, M. M. Marinak, P. K. Patel, H. F. Robey, and S. M. Sepke, High-resolution, detailed simulations of low foot and high foot implosion experiments on the NIF (2015), 57th Annual Meeting of the APS Division of Plasma Physics, Vol. 60 (2015), http://meetings.aps.org/link/BAPS.2015.DPP.CI3.1.
[67] D. S. Clark, D. E. Hinkel, D. C. Eder, O. S. Jones, S. W. Haan, B. A. Hammel, M. M. Marinak, J. L. Milovich, H. F. Robey, L. J. Suter, and R. P. J. Town, Phys. Plasmas **20**, 056318 (2013).
[68] C. Cerjan, P. T. Springer, and S. M. Sepke, Phys. Plasmas **20**, 056319 (2013).
[69] B. A. Remington, L. J. Atherton, L. R. Benedett, L. Berzak-Hopkins, D. K. Bradley, D. A. Callahan, D. T. Casey, P. M. Celliers, C. J. Cerjan, D. S. Clark, E. L. Dewald, T. R. DFittrich, S. N. Dixit, F. Doppner, D. H. Edgell, M. J. Edwards, R. Epstein, J. Frenje, M. Gatu-Johnson, S. Glenn, S. H. Glenzer, G. Grim, S. W. Haan, B. A. Hammel, A. Hamza, D. Hicks, W. W. Hsing, O. Hurricane, N. Izumi, O. S. Jones, M. H. Key, S. F. Khan, J. D. Kilkenny, G. A. Kyrala, O. L. Landen, S. LePape, J. D. Lindl, T. Ma, B. J. MacGowen, A. J. Mackinnon, A. G. MacPhee, N. B. Meezan, J. D. Moody, E. I. Moses, A. Nikroo, A. Pak, T. Parham, H.-S. Park, P. K. Patel, R. Petrasso, J. Pino, J. E. Ralph, K. Raman, S. P. Regan, H. F. Robey, J. S. Ross, B. K. Spears, V. A. Smalyuk, P. T. Springer, I. J. Suter, R. Tipton, R. Tommasim, R. P. Town, and S. V. Weber, J. Phys.: Conf. Ser. **688**, 012090 (2016).
[70] C. R. Weber, D. S. Clark, A. W. Cook, D. C. Eder, S. W. Haan, B. A. Hammel, D. E. Hinkel, O. S. Jones, M. M. Marinak, J. L. Milovich, P. K. Patel, H. F. Robey, J. D. Salmonson, S. M. Sepke, and C. A. Thomas, Phys. Plasmas **22**, 032702 (2015).
[71] S. Mitchell and M. Vynnycky, J. Comput. Appl. Math. **236**, 4181 (2012).